J. Fluid Mech. (2001), *vol.* 432, *pp.* 313–339. Printed in the United Kingdom

Longitudinal vortices in a laminar natural convection boundary layer flow on an inclined flat plate and their influence on heat transfer

By PETER JESCHKE AND HANS BEER

Institut für Technische Thermodynamik, Technische Universität Darmstadt, Petersenstr. 30, D-64287 Darmstadt, Germany

(Received 14 December 1999 and in revised form 24 August 2000)

The linear and nonlinear growth of longitudinal vortices in a laminar boundary layer and the development of secondary instabilities are investigated theoretically and by experiment. As a prototype problem the natural convection flow along a constant-heat-flux inclined flat plate in water is chosen. Based upon the smallness of the plate's angle of inclination from the vertical, the largeness of the Grashof number, and the smallness of the vortex strength, a perturbation method is used to derive and solve a consistent set of governing equations for the linear, weakly nonlinear and the strongly nonlinear regimes which is asymptotically correct to first order. Liquid-crystal thermography based on wide-band liquid crystals is used to provide full-field, highly accurate wall temperature measurements and visualizations.

The spanwise periodic thickening and thinning of the boundary layer through a nonlinear, but steady, vortex growth is seen to be responsible for practically all of the increase of mean heat transfer values during the laminar–turbulent transition. Secondary instabilties in the form of sinuous and varicose unsteady wave modes and the steady merging of vortices are visualized but are seen to have only a minor additional influence on mean heat transfer.

1. Introduction

Two-dimensional laminar boundary layers may become unstable with respect to three-dimensional disturbances in the form of steady, streamwise-oriented, and counter-rotating vortices (see figure 1). Well known are the Taylor (Taylor 1923), Dean (Dean 1928) and Görtler vortices (Görtler 1940), which are caused by a centrifugal instability, as well as the longitudinal vortices appearing in mixed (Görtler 1958) and natural convection flows (Sparrow & Husar 1969) as result of a buoyancy-induced instability. Through a nonlinear distortion of the boundary layer these longitudinal vortices may increase mean values of skin friction and heat transfer several times compared to the undisturbed values. Whereas the increase in skin friction is generally a disadvantage in technical applications the increased heat transfer can be exploited in some applications such as heat exchangers, but should be avoided in others such as gas turbine applications, for instance. Besides these direct effects, the longitudinal vortices may indirectly lead to a laminar–turbulent transition in the nonlinear regime by destabilizing rapidly growing secondary instabilities which finally lead to turbulence. Therefore, the appearance of longitudinal vortices in a laminar boundary layer is generally an indicator of forthcoming turbulence.

For the case of a natural convection boundary layer flow along an inclined flat plate

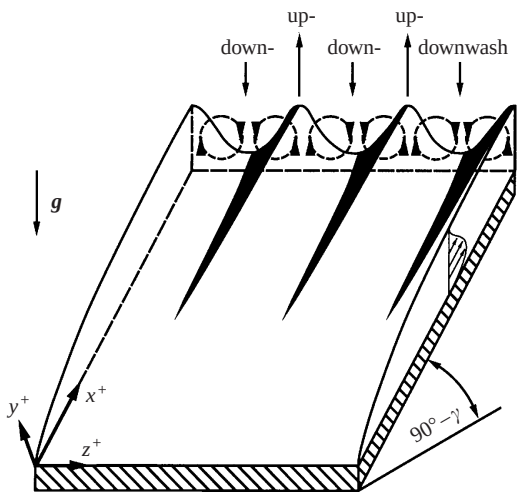

FIGURE 1. Longitudinal vortices in a laminar natural convection boundary-layer flow along a heated inclined flat plate. Black shades are used to show the boundary-layer's wavy structure.

an attempt will be made here to investigate the nonlinear effects of the vortex, with special emphasis on heat transfer. Until now, no nonlinear theoretical investigation capable of determining the velocity and temperature profiles in the nonlinear regime, which give rise to the increase of mean values, has existed for this case, to the authors' knowledge. Also, no experimental heat transfer data suitable for detailed comparison with theoretical results are available. This paper is, therefore, devoted to both of these tasks. Further cases are investigated in a similar manner by Jeschke (1998). These are the Görtler case of a forced convection flow along a curved wall and the case of a mixed convection flow along a flat plate.

Sparrow & Husar (1969), Lloyd & Sparrow (1970), and Lloyd (1974) were the first to prove experimentally the existence of longitudinal vortices in a natural convection flow along an inclined flat plate. With an electrochemical flow visualization they were able to identify longitudinal vortices in their water flow for inclination angles of 17° or greater from the vertical whereas the mode of instability for angles of 14° or less was a two-dimensional wave structure. In between 14° and 17° both modes were found to coexist. However, even though these experiments showed the existence of longitudinal vortices in a natural convection flow along inclined surfaces, there were several later heat transfer measurements (Fujii & Imura 1972; Pera & Gebhart 1973; Black & Norris 1975; Vliet & Ross 1975; King & Reible 1991) with no explicit identification of such vortices. The same is true for several investigations of natural convection flows along heated horizontal surfaces (Goldstein, Sparrow & Jones 1973; Lloyd & Moran 1974; Yousef, Tarasuk & McKeen 1982; Kitamura & Kimura 1995) for which the buoyancy force destabilizes the flow in an analogous way. However, in the liquid crystal visualizations of Kitamura & Kimura (1995) the vortices' influence can clearly be identified. Cheng & Kim (1988) have shown by smoke visualizations that longitudinal vortices do indeed exist in such an environment. The only known measurements explicitly investigating the influence of the vortices on heat transfer along an inclined flat plate are due to Shaukatullah & Gebhart (1978). Using embedded thermocouples in their constant-heat-flux plate as well as thermocouples and hot-film anemometers on a traversing mechanism they measured heat transfer coefficients as well as temperatures and velocity profiles within the boundary layer

in a water flow for inclination angles between 14° and 29° from the vertical. They concluded from their velocity measurements that the modification of the temperature profiles is due to the existence of a longitudinal vortex system. However, owing to the use of thermocouples, the resolution of the spanwise measurements of the boundary-layer temperatures across one vortex pair with a wavelength of approximately 1 cm was limited. Also, the downstream heat transfer data were not sufficient to record the development of mean values during the transition process. Zuercher, Jacobs & Chen (1998) have recently experimentally investigated the secondary instabilities of longitudinal vortices along an isothermal plate in water. Using a schlieren visualization technique they identified as the dominant secondary instability effect a merging of the schlieren streaks that correspond to the vortices' hot upwash legs. Unsteady wave modes just before 'vortex merger' were also identified.

For the natural convection case treated here the previous theoretical work has been limited to the primary stability problem, with the exception of that of Chen *et al.* (1991) who investigated vortex merger as a secondary stability problem. The traditional technique for the primary stability problem had been the solution of a normal-mode eigenvalue problem until Hall (1983) showed that in Görtler flow, apart from the high-wavenumber limit, use of the normal-mode eigenvalue solution cannot be justified to find neutral stability. The same argument should also apply for the natural convection case due to the similarity of the two. However, for the natural convection case only linear eigenvalue approaches exist, the first of which were normal-mode analyses carried out by Haaland & Sparrow (1973) and Hwang & Cheng (1973). Both determined stability diagrams whose critical point disagreed by several orders of magnitude with values extracted from experimental data. Further linear eigenvalue approaches were made by Kahawita & Meroney (1974), Iyer & Kelly (1974), Chen & Tzuoo (1982), Tien, Chen & Armaly (1986), and Lee, Chen & Armaly (1992) sometimes with different terms in the disturbance equations to attempt to take correct account of the non-parallelism of the basic flow. Chen *et al.* (1991) solved governing equations for the nonlinear evolution of the vortex rolls that essentially were nonlinear extensions of those from Haaland & Sparrow (1973), i.e. they imposed a modified parallel flow approximation. Owing to the omission of the interaction between the vortical disturbances and the mean flow, their nonlinear theory was not able to predict any increase in integral parameters such as mean heat transfer values.

The theoretical approach of this study (§ 2) makes use of a perturbation method to derive a consistent set of governing equations for the linear, weakly nonlinear and strongly nonlinear regimes which is asymptotically correct to first order. The theory and the resulting equations for the linear regime are analogous to those of Hall (1983) for the Görtler case and Hall & Morris (1992) for the heated Blasisus case. The weakly nonlinear analysis is new, whereas the theory and governing equations for the strongly nonlinear regime are again analogous to those of Hall (1988) for the Görtler case and can be compared to Hall's (1993) high-wavenumber theory for the heated Blasius case. Our solution procedure for the governing equations is similar to that used by Lee & Liu (1992) and Liu & Lee (1995) for the Görtler case and the heated Blasius case, respectively. The experimental procedure of this study (§ 3) is thermochromic liquid crystal (TLC) thermography which is described in detail in Jeschke, Biertümpfel & Beer (2000). The steady-state constant-heat-flux method using wide-band TLCs is applied which provides full-field and high-resolution heat transfer results and wall temperature visualizations. The vortices' effect on the kinematics of the flow, their influence on wall heat transfer and the experimentally observed

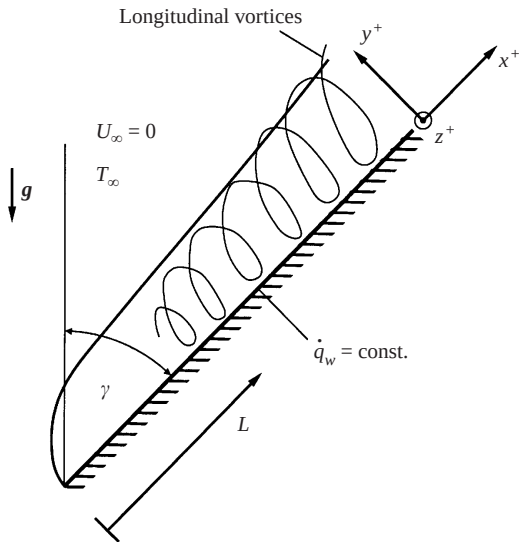

FIGURE 2. Sketch of the problem.

secondary instabilities are presented (§4). A thorough description of the theoretical and experimental methods as well as the results is given in Jeschke (1998).

2. Theoretical method

2.1. *Formulation of the problem*

A laminar natural convection boundary layer flow along an inclined constant-heat-flux plate is considered with boundary conditions as specified in figure 2. There, the plate inclination angle γ, the specific wall heat flux $\dot{q}_w$, the wall surface temperature T_w, the far-field temperature T_∞, the far-field velocity U_∞, and the dimensional Cartesian coordinates $\{x^+, y^+, z^+\}$ are identified. Naturally occurring longitudinal vortices, i.e. triggered by infinitesimally small disturbances, are assumed to develop on top of the otherwise two-dimensional boundary layer flow in the case of instability. The dimensionless amplitude ϵ of the vortices is therefore assumed to be small initially. In addition, the plate is set to be almost parallel to the gravitational vector $\boldsymbol{g}$, and the Grashof number Gr_L^*, evaluated at a downstream distance L which is characteristic of the locus of vortex inception, is considered to be large, while the stability parameter N_L^* is fixed to be finite in agreement with the experimental results. The Prandtl number Pr is taken to be finite too. Thus, the problem is taken to be characterized by

$$Gr_L^* = \frac{\beta \dot{q}_w g \cos\gamma L^4}{\lambda \nu^2} \to \infty, \quad \tan\gamma \to 0, \quad \epsilon \to 0, \tag{2.1}$$

$$N_L^* = \tan\gamma Gr_L^{*\,1/5}, \quad Pr = \frac{\eta c_p}{\lambda} \quad \text{fixed.} \tag{2.2}$$

β is the coefficient of thermal expansion, λ the thermal conductivity, c_p the specific heat at constant pressure, ν the kinematic viscosity, and η the dynamic viscosity. The Grashof number is based on $g\cos\gamma$ since in the limits of equation (2.1) the solution is then not explicitly dependent upon γ but only implicitly upon Gr_L^* and N_L^* as defined in equations (2.1) and (2.2).

The primary reference lengthscale is L and the primary reference velocity deter-

mined from a balance of the driving effects, i.e. buoyancy and convection for the x^+-momentum, is $U_{typ} = \sqrt{\beta(T_w - T_\infty)_{typ} g \cos\gamma L}$ while the primary reference temperature change $(T_w - T_\infty)_{typ} = \dot{q}_w L Gr_L^{*-1/5}/\lambda$ can be estimated *a posteriori* from the inner solution satisfying the constant-heat-flux wall boundary condition (Jeschke 1998). Using L and U_{typ} one arrives at the dimensionless coordinates $\{X, Y, Z\}$ and the corresponding velocity components $\{U, W, V\}$, respectively. The dimensionless pressure follows from $P = p^+/(\rho U_{typ}^2)$ and the dimensionless temperature from $T = (T^+ - T_\infty)/(T_w - T_\infty)_{typ}$ with p^+, T^+, and ρ being the dimensional pressure, dimensional temperature, and density, respectively.

Starting from the steady Boussinesq equations in Cartesian coordinates, the governing equations comprising equations for the conservation of mass, momentum, and energy then are

$$\frac{\partial U}{\partial X} + \frac{\partial V}{\partial Y} + \frac{\partial W}{\partial Z} = 0, \tag{2.3}$$

$$U\frac{\partial U}{\partial X} + V\frac{\partial U}{\partial Y} + W\frac{\partial U}{\partial Z} = -\frac{\partial P}{\partial X} + T + Gr_L^{*-2/5}\left[\frac{\partial^2 U}{\partial X^2} + \frac{\partial^2 U}{\partial Y^2} + \frac{\partial^2 U}{\partial Z^2}\right], \tag{2.4}$$

$$U\frac{\partial V}{\partial X} + V\frac{\partial V}{\partial Y} + W\frac{\partial V}{\partial Z} = -\frac{\partial P}{\partial Y} + \tan\gamma\, T + Gr_L^{*-2/5}\left[\frac{\partial^2 V}{\partial X^2} + \frac{\partial^2 V}{\partial Y^2} + \frac{\partial^2 V}{\partial Z^2}\right], \tag{2.5}$$

$$U\frac{\partial W}{\partial X} + V\frac{\partial W}{\partial Y} + W\frac{\partial W}{\partial Z} = -\frac{\partial P}{\partial Z} + Gr_L^{*-2/5}\left[\frac{\partial^2 W}{\partial X^2} + \frac{\partial^2 W}{\partial Y^2} + \frac{\partial^2 W}{\partial Z^2}\right], \tag{2.6}$$

$$U\frac{\partial T}{\partial X} + V\frac{\partial T}{\partial Y} + W\frac{\partial T}{\partial Z} = Pr^{-1} Gr_L^{*-2/5}\left[\frac{\partial^2 T}{\partial X^2} + \frac{\partial^2 T}{\partial Y^2} + \frac{\partial^2 T}{\partial Z^2}\right], \tag{2.7}$$

with wall condition:

$$U = V = W = 0, \quad \frac{\partial T}{\partial Y} = -Gr_L^{*1/5} \quad \text{for} \quad Y = 0,\ X \geqslant 0, \tag{2.8}$$

and upstream condition:

$$U = V = W = T = 0 \quad \text{for } X \to -\infty \tag{2.9}$$

The boundary conditions are specified according to figure 2.

For the weakly nonlinear and the nonlinear downstream calculation initial conditions must be specified. But in the case of naturally occurring vortices, neither the vortex origin nor the initial vortex strength are known since the vortices are triggered randomly. However, any infinitesimally small initial disturbances will develop into vortices according to the linear stability solution governed by equations (2.27)–(2.34) from which the disturbance quantities u_{st}, v_{st}, w_{st}, t_{st} and the relative scaling of the cross-stream velocities in equations (2.10)–(2.13) can be taken. But the amplitude ϵ up to which the vortices have grown at $x^+ = L$ is a function of the triggering and can therefore only be supplied by comparison with experiment. For our calculations, ϵ and L are chosen to achieve best agreement between theory and experiment for the location where the mean Nusselt numbers deviate from the basic flow values (cf. figure 11), thereby indirectly providing this necessary initial information. The initial conditions can then be specified as

$$U(X = 1, Y, Z) = U_{gr}(X = 1, Y) + \epsilon u_{st}(X = 1, y, z), \tag{2.10}$$

$$V(X = 1, Y, Z) = V_{gr}(X = 1, Y) + \epsilon Gr_L^{*-1/5} v_{st}(X = 1, y, z), \tag{2.11}$$

$$W(X=1,Y,Z) = W_{gr}(X=1,Y) + \epsilon Gr_L^{*\,-1/5} w_{st}(X=1,y,z), \tag{2.12}$$

$$T(X=1,Y,Z) = T_{gr}(X=1,Y) + \epsilon t_{st}(X=1,y,z), \tag{2.13}$$

with

$$U_{gr}, V_{gr}, \ldots, u_{st}, v_{st}, \ldots = O(1).$$

U_{gr}, V_{gr}, W_{gr}, T_{gr} are the basic flow quantities and y, z are defined below in equations (2.14) and (2.15).

2.2. *Linear and weakly nonlinear approximation*

The formulated problem comprises a multiple-limit perturbation problem associated with the perturbation quantities Gr_L^*, $\tan\gamma$, and ϵ. N_L^* is the similarity parameter which, in combination with equation (2.2), specifies the relative rates at which Gr_L^* and $\tan\gamma$ approach their limits. In effect, the independent limits $\epsilon \to 0$ and $Gr_L^* \to \infty$ remain. The former leads to a regular perturbation problem whereas the latter results in a singular one which is solved using the method of matched asymptotic expansions. Since the Grashof number is typically very large it is sufficient to consider only the leading term of the expansion in Gr_L^* and disregard terms of $O(Gr_L^{*\,-1/5})$ or less whereas for the expansion in ϵ a five-term expansion is carried out within the scope of the weakly nonlinear approach and no expansion is made within the scope of the strongly nonlinear approach. This accounts for the fact that the disturbance amplitude grows starting from an infinitesimally small value up to order-one values as the vortices move downstream.

Up to the leading term in Gr_L^* the outer expansion gives the trivial solution of a quiescent fluid of constant pressure at far-field temperature. However, owing to the loss of the highest derivatives, the outer solution becomes singular at $Y \to 0$ where it cannot satisfy the temperature boundary condition. In this region of non-uniformity the inner problem is constructed where independent and dependent variables are denoted by lower-case letters. Stretching the wall-normal coordinate by

$$y = Y\, Gr_L^{*\,1/5} \quad \text{with } y = O(1) \tag{2.14}$$

then leads to an inner solution that does not share the outer solution's degeneracy. Since the typical lengthscales of the vortical disturbances are equal in the wall-normal and spanwise direction it also follows that

$$z = Z\, Gr_L^{*\,1/5} \quad \text{with } z = O(1). \tag{2.15}$$

Substituting equations (2.14), (2.15) into (2.3)–(2.9) and replacing

$$\tan\gamma = N_L^* Gr_L^{*\,-1/5}, \tag{2.16}$$

then leads to the inner equations being a function of only ϵ and Gr_L^* for which all dependent variables can be expanded:

$$U = u_1^0 + \epsilon u_1^* + \epsilon^2 u_1^{**} + \cdots + Gr_L^{*\,-1/5}[u_2^0 + \epsilon u_2^* + \epsilon^2 u_2^{**} + \cdots] + \cdots, \tag{2.17}$$

$$V = v_1^0 + \epsilon v_1^* + \epsilon^2 v_1^{**} + \cdots + Gr_L^{*\,-1/5}[v_2^0 + \epsilon v_2^* + \epsilon^2 v_2^{**} + \cdots] + \cdots, \tag{2.18}$$

$$W = 0 + \epsilon w_1^* + \epsilon^2 w_1^{**} + \cdots + Gr_L^{*\,-1/5}[0 + \epsilon w_2^* + \epsilon^2 w_2^{**} + \cdots] + \cdots, \tag{2.19}$$

$$P = p_1^0 + \epsilon p_1^* + \epsilon^2 p_1^{**} + \cdots + Gr_L^{*\,-1/5}[p_2^0 + \epsilon p_2^* + \epsilon^2 p_2^{**} + \cdots] + \cdots, \tag{2.20}$$

$$T = t_1^0 + \epsilon t_1^* + \epsilon^2 t_1^{**} + \cdots + Gr_L^{*\,-1/5}[t_2^0 + \epsilon t_2^* + \epsilon^2 t_2^{**} + \cdots] + \cdots, \tag{2.21}$$

with

$$u_1^0, u_1^*, \ldots, v_1^0, v_1^*, \ldots = O(1),$$

and

$$X, y, z = O(1), \quad Gr_L^* \to \infty, \quad \epsilon \to 0.$$

Here it is anticipated that, for the given boundary conditions, the basic solution variables (denoted by ^{0}) will be functions only of (X, y) with no spanwise velocity component whereas all higher-order variables are functions of (X, y, z) in general.

Substituting (2.17)–(2.21) into (2.3)–(2.13), taking the limits (2.1), (2.2), using the already known outer solution, and applying the asymptotic matching principle of Van Dyke (1975) to provide boundary conditions at $y \to \infty$, then leads to the approximations given below in a strictly formal manner (see Jeschke 1998).

2.2.1. *Zeroth-order, basic solution*

According to the expansion (2.17)–(2.21), the zeroth-order variables are u_1^0, v_1^0, p_1^0, t_1^0. The formal procedure leads to $v_1^0 = 0$, $p_1^0 = const$ and gives u_1^0, t_1^0 as a solution to

$$\frac{\partial u_1^0}{\partial X} + \frac{\partial v_2^0}{\partial y} = 0, \tag{2.22}$$

$$u_1^0 \frac{\partial u_1^0}{\partial X} + v_2^0 \frac{\partial u_1^0}{\partial y} - t_1^0 - \frac{\partial^2 u_1^0}{\partial y^2} = 0, \tag{2.23}$$

$$u_1^0 \frac{\partial t_1^0}{\partial X} + v_2^0 \frac{\partial t_1^0}{\partial y} - Pr^{-1} \frac{\partial^2 t_1^0}{\partial y^2} = 0, \tag{2.24}$$

with wall condition

$$u_1^0 = v_2^0 = 0, \quad \frac{\partial t_1^0}{\partial y} = -1, \quad \text{for } X \geqslant 0,\ y = 0, \tag{2.25}$$

and matching condition

$$u_1^0 = t_1^0 = 0 \quad \text{for } y = \infty. \tag{2.26}$$

Equations (2.22)–(2.24) arise from the continuity, X-momentum, and energy equations, respectively, and are formally identical with the equations for a natural convection flow along a vertical plate. v_2^0 appears in equations (2.22)–(2.24) and must therefore be solved for, but has only a higher-order contribution of $O({Gr_L^*}^{-1/5})$ which was neglected. The wall-normal buoyancy appears to leading order within the equation

$$u_1^0 \frac{\partial v_2^0}{\partial X} + v_2^0 \frac{\partial v_2^0}{\partial y} - N_L^* t_1^0 + \frac{\partial p_3^0}{\partial y} - \frac{\partial^2 v_2^0}{\partial y^2} = 0$$

(Jeschke 1998). However, since u_1^0, v_2^0, and t_1^0 are known from (2.22)–(2.26) this equation merely determines p_3^0 which has the neglected higher-order contribution of $O({Gr_L^*}^{-2/5})$. Equations (2.22)–(2.26) without wall-normal buoyancy, therefore, indeed comprise the consistent zeroth-order approximation. Since the term $N_L^* t_1^*$ appears in equation (2.29) this is surprising, nevertheless correct. Equations (2.22)–(2.26) are readily solved by a similarity solution in combination with a numerical Runge–Kutta shooting method.

2.2.2. *First-order, linear solution*

In the linear problem the $O(\epsilon)$ terms in (2.17)–(2.21), i.e. u_1^*, v_1^*, w_1^*, p_1^*, and t_1^* are solved for. Applying the formal perturbation method it is seen that $v_1^* = w_1^* = p_1^* = 0$ and that u_1^*, t_1^* must be determined from the following system of equations arising from the continuity, X-, y-, z-momentum, and the energy equations:

$$\frac{\partial u_1^*}{\partial X} + \frac{\partial v_2^*}{\partial y} + \frac{\partial w_2^*}{\partial z} = 0, \tag{2.27}$$

$$u_1^0 \frac{\partial u_1^*}{\partial X} + u_1^* \frac{\partial u_1^0}{\partial X} + v_2^0 \frac{\partial u_1^*}{\partial y} + v_2^* \frac{\partial u_1^0}{\partial y} - t_1^* - \frac{\partial^2 u_1^*}{\partial y^2} - \frac{\partial^2 u_1^*}{\partial z^2} = 0, \tag{2.28}$$

$$u_1^0 \frac{\partial v_2^*}{\partial X} + u_1^* \frac{\partial v_2^0}{\partial X} + v_2^0 \frac{\partial v_2^*}{\partial y} + v_2^* \frac{\partial v_2^0}{\partial y} - N_L^* t_1^* + \frac{\partial p_3^*}{\partial y} - \frac{\partial^2 v_2^*}{\partial y^2} - \frac{\partial^2 v_2^*}{\partial z^2} = 0, \tag{2.29}$$

$$u_1^0 \frac{\partial w_2^*}{\partial X} + v_2^0 \frac{\partial w_2^*}{\partial y} + \frac{\partial p_3^*}{\partial z} - \frac{\partial^2 w_2^*}{\partial y^2} - \frac{\partial^2 w_2^*}{\partial z^2} = 0, \tag{2.30}$$

$$u_1^0 \frac{\partial t_1^*}{\partial X} + u_1^* \frac{\partial t_1^0}{\partial X} + v_2^0 \frac{\partial t_1^*}{\partial y} + v_2^* \frac{\partial t_1^0}{\partial y} - Pr^{-1} \frac{\partial^2 t_1^*}{\partial y^2} - Pr^{-1} \frac{\partial^2 t_1^*}{\partial z^2} = 0, \tag{2.31}$$

with upstream condition

$$u_1^* = u_{st}, \quad v_2^* = v_{st}, \quad w_2^* = w_{st}, \quad t_1^* = t_{st}, \quad \text{for } X = 1, \tag{2.32}$$

wall condition

$$u_1^* = v_2^* = w_2^* = \frac{\partial t_1^*}{\partial y} = 0 \quad \text{for } y = 0, \tag{2.33}$$

and matching condition

$$u_1^* = \frac{\partial v_2^*}{\partial y} = w_2^* = t_1^* = 0 \quad \text{for } y = \infty. \tag{2.34}$$

Similar to the above, v_2^*, w_2^*, and p_3^* appear in equations (2.27)–(2.34) and must be solved for; their solution can be disregarded however since these terms are of $O(\epsilon Gr_L^{*\,-1/5})$ and $O(\epsilon Gr_L^{*\,-2/5})$, respectively. Equations (2.27)–(2.34) are linear because the basic flow is known from equations (2.22)–(2.26) and are susceptible to a downstream marching solution scheme, since the perturbation method has changed the type of the differential equations to become parabolic in the downstream direction. The marching solution is carried out using the SIMPLER (Patankar 1980) finite volume procedure.

2.2.3. *Second order*

In the second-order problem a solution is sought to the $O(\epsilon^2)$ terms in (2.17)–(2.21), i.e. for u_1^{**}, v_1^{**}, w_1^{**}, p_1^{**}, and t_1^{**}. Similar to the above, one immediately arrives at $v_1^{**} = w_1^{**} = p_1^{**} = 0$, and u_1^{**}, t_1^{**} must be determined from

$$\frac{\partial u_1^{**}}{\partial X} + \frac{\partial v_2^{**}}{\partial y} + \frac{\partial w_2^{**}}{\partial z} = 0, \tag{2.35}$$

$$u_1^0 \frac{\partial u_1^{**}}{\partial X} + u_1^{**} \frac{\partial u_1^0}{\partial X} + v_2^0 \frac{\partial u_1^{**}}{\partial y} + v_2^{**} \frac{\partial u_1^0}{\partial y} - t_1^{**} - \frac{\partial^2 u_1^{**}}{\partial y^2} - \frac{\partial^2 u_1^{**}}{\partial z^2} = -u_1^* \frac{\partial u_1^*}{\partial X} - v_2^* \frac{\partial u_1^*}{\partial y} - w_2^* \frac{\partial u_1^*}{\partial z}, \tag{2.36}$$

$$u_1^0\frac{\partial v_2^{**}}{\partial X}+u_1^{**}\frac{\partial v_2^0}{\partial X}+v_2^0\frac{\partial v_2^{**}}{\partial y}+v_2^{**}\frac{\partial v_2^0}{\partial y}-N_L^*t_1^{**}+\frac{\partial p_3^{**}}{\partial y}-\frac{\partial^2 v_2^{**}}{\partial y^2}-\frac{\partial^2 v_2^{**}}{\partial z^2}$$
$$=-u_1^*\frac{\partial v_2^*}{\partial X}-v_2^*\frac{\partial v_2^*}{\partial y}-w_2^*\frac{\partial v_2^*}{\partial z}, \quad (2.37)$$

$$u_1^0\frac{\partial w_2^{**}}{\partial X}+v_2^0\frac{\partial w_2^{**}}{\partial y}+\frac{\partial p_3^{**}}{\partial z}-\frac{\partial^2 w_2^{**}}{\partial y^2}-\frac{\partial^2 w_2^{**}}{\partial z^2}$$
$$=-u_1^*\frac{\partial w_2^*}{\partial X}-v_2^*\frac{\partial w_2^*}{\partial y}-w_2^*\frac{\partial w_2^*}{\partial z}, \quad (2.38)$$

$$u_1^0\frac{\partial t_1^{**}}{\partial X}+u_1^{**}\frac{\partial t_1^0}{\partial X}+v_2^0\frac{\partial t_1^{**}}{\partial y}+v_2^{**}\frac{\partial t_1^0}{\partial y}-Pr^{-1}\frac{\partial^2 t_1^{**}}{\partial y^2}-Pr^{-1}\frac{\partial^2 t_1^{**}}{\partial z^2}$$
$$=-u_1^*\frac{\partial t_1^*}{\partial X}-v_2^*\frac{\partial t_1^*}{\partial y}-w_2^*\frac{\partial t_1^*}{\partial z}, \quad (2.39)$$

with upstream condition

$$u_1^{**}=v_2^{**}=w_2^{**}=t_1^{**}=0 \quad \text{for } X=1, \quad (2.40)$$

wall condition

$$u_1^{**}=v_2^{**}=w_2^{**}=\frac{\partial t_1^{**}}{\partial y}=0 \quad \text{for } y=0, \quad (2.41)$$

and matching condition

$$u_1^{**}=\frac{\partial v_2^{**}}{\partial y}=w_2^{**}=t_1^{**}=0 \quad \text{for } y=\infty. \quad (2.42)$$

Again, (2.35)–(2.42) are a set of linear differential equations parabolic in the downstream direction which are readily solved using the above mentioned marching scheme, after the first-order variables are determined.

2.2.4. *Third, fourth order*

Equations up to the fourth order are derived and successively solved using the marching scheme. The linear nature all of those ensures a rapid numerical solution. However, from fourth order on the increasing number of successive problems to be solved no longer leads to any improvement in computation time over the strongly nonlinear approach presented in § 2.3. Nevertheless, the five-term weakly nonlinear approach enables a solution through almost all of the transition regime up to the appearance of unsteady secondary instabilities which cannot be captured by the steady approaches presented herein anyway.

The weakly nonlinear solution of the inner problem can be summarized as

$$U=u_1^0+\epsilon u_1^*+\epsilon^2 u_1^{**}+\cdots+O(Gr_L^{*\,-1/5}), \quad (2.43)$$

$$V=0+O(Gr_L^{*\,-1/5}), \quad (2.44)$$

$$W=0+O(Gr_L^{*\,-1/5}), \quad (2.45)$$

$$P=\text{const.}+O(Gr_L^{*\,-1/5}), \quad (2.46)$$

$$T=t_1^0+\epsilon t_1^*+\epsilon^2 t_1^{**}+\cdots+O(Gr_L^{*\,-1/5}), \quad (2.47)$$

with

$$X, y, z, \text{ const.} = O(1).$$

Even though the cross-stream velocities of $O(Gr_L^{*-1/5})$ or smaller are calculated, they are not listed here for consistency reasons, since U and T are not determined to this high order. However, the solution to these higher-order cross-stream velocities is discussed in § 4.2 (cf. figure 5*a*).

Let $h = \dot{q}_w/(T_w - T_\infty)$ be the heat transfer coefficient; then local Nusselt numbers $Nu = hx^+/\lambda$ follow from

$$Nu = Gr_L^{*1/5} X\{t_1^0(X,0) + \epsilon t_1^*(X,0,z) + \epsilon^2 t_1^{**}(X,0,z) + \cdots + O(Gr_L^{*-1/5})\}^{-1} \tag{2.48}$$

and local Nusselt numbers for the unperturbed basic solution from

$$Nu_{gr} = Gr_L^{*1/5} X \frac{1}{t_1^0(X,0)}. \tag{2.49}$$

Local Grashof numbers $Gr^* = \beta \dot{q}_w g \cos\gamma x^{+4}/(\lambda v^2)$ and stability parameters $N^* = \tan\gamma Gr^{*1/5}$ are determined from the corresponding parameters evaluated at L by

$$Gr^* = Gr_L^* X^4, \tag{2.50}$$

$$N^* = N_L^* X^{4/5}. \tag{2.51}$$

2.3. *Strongly nonlinear approximation*

Near the end of the transition regime the vortical disturbances acquire amplitudes of the order of the basic flow values so that the limit $\epsilon \to 0$ is not justified anymore. Only the singular perturbation problem associated with $Gr_L^* \to \infty$ remains. Again, the method of matched asymptotic expansions can be formally applied to derive a consistent set of governing equations to the leading order in Gr_L^*.

As above, up to the leading term in Gr_L^* the outer expansion gives the trivial solution. The inner solution is constructed as described by equations (2.14)–(2.16) and the dependent variables can be expanded as

$$U = u_1^0 + u_1^* + Gr_L^{*-1/5}[u_2^0 + u_2^*] + \cdots, \tag{2.52}$$

$$V = v_1^0 + v_1^* + Gr_L^{*-1/5}[v_2^0 + v_2^*] + \cdots, \tag{2.53}$$

$$W = 0 + w_1^* + Gr_L^{*-1/5}[0 + w_2^*] + \cdots, \tag{2.54}$$

$$P = p_1^0 + p_1^* + Gr_L^{*-1/5}[p_2^0 + p_2^*] + \cdots, \tag{2.55}$$

$$T = t_1^0 + t_1^* + Gr_L^{*-1/5}[t_2^0 + t_2^*] + \cdots, \tag{2.56}$$

with

$$u_1^0, u_1^*, \ldots, v_1^0, v_1^*, \ldots = O(1)$$

and

$$X, y, z = O(1), \quad Gr_L^* \to \infty.$$

In (2.52)–(2.56), for mathematical convenience the dependent variables are split into the basic solution variables (denoted by ^{0}), being functions of (X, y) with no spanwise velocity component, and the disturbance variables (denoted by *), being functions of (X, y, z). No assumption is made about the smallness of the disturbances relative to the basic flow.

Substituting (2.52)–(2.56) into (2.3)–(2.13), taking the limits (2.1), (2.2) (except $\epsilon \to 0$) and carrying out the same procedure as above then leads to the zeroth-order approximations given below (see Jeschke 1998).

2.3.1. *Zeroth order*

In the zeroth-order problem a solution is sought to the $O(1)$ terms in (2.52)–(2.56). One immediately arrives at $v_1^0 = 0$, $p_1^0 = \text{const}$, and u_1^0, t_1^0 are governed by a set of equations formally identical with (2.22)–(2.26). Thereby, the basic flow solution is identical to the above. For the disturbance quantities one finds $v_1^* = w_1^* = p_1^* = 0$, and for u_1^* and t_1^* the set of equations

$$\frac{\partial u_1^*}{\partial X} + \frac{\partial v_2^*}{\partial y} + \frac{\partial w_2^*}{\partial z} = 0, \tag{2.57}$$

$$u_1^0 \frac{\partial u_1^*}{\partial X} + u_1^* \frac{\partial u_1^0}{\partial X} + v_2^0 \frac{\partial u_1^*}{\partial y} + v_2^* \frac{\partial u_1^0}{\partial y} - t_1^* - \frac{\partial^2 u_1^*}{\partial y^2} - \frac{\partial^2 u_1^*}{\partial z^2} = -u_1^* \frac{\partial u_1^*}{\partial X} - v_2^* \frac{\partial u_1^*}{\partial y} - w_2^* \frac{\partial u_1^*}{\partial z}, \tag{2.58}$$

$$u_1^0 \frac{\partial v_2^*}{\partial X} + u_1^* \frac{\partial v_2^0}{\partial X} + v_2^0 \frac{\partial v_2^*}{\partial y} + v_2^* \frac{\partial v_2^0}{\partial y} - N_L^* t_1^* + \frac{\partial p_3^*}{\partial y} - \frac{\partial^2 v_2^*}{\partial y^2} - \frac{\partial^2 v_2^*}{\partial z^2} = -u_1^* \frac{\partial v_2^*}{\partial X} - v_2^* \frac{\partial v_2^*}{\partial y} - w_2^* \frac{\partial v_2^*}{\partial z}, \tag{2.59}$$

$$u_1^0 \frac{\partial w_2^*}{\partial X} + v_2^0 \frac{\partial w_2^*}{\partial y} + \frac{\partial p_3^*}{\partial z} - \frac{\partial^2 w_2^*}{\partial y^2} - \frac{\partial^2 w_2^*}{\partial z^2} = -u_1^* \frac{\partial w_2^*}{\partial X} - v_2^* \frac{\partial w_2^*}{\partial y} - w_2^* \frac{\partial w_2^*}{\partial z}, \tag{2.60}$$

$$u_1^0 \frac{\partial t_1^*}{\partial X} + u_1^* \frac{\partial t_1^0}{\partial X} + v_2^0 \frac{\partial t_1^*}{\partial y} + v_2^* \frac{\partial t_1^0}{\partial y} - Pr^{-1} \frac{\partial^2 t_1^*}{\partial y^2} - Pr^{-1} \frac{\partial^2 t_1^*}{\partial z^2} = -u_1^* \frac{\partial t_1^*}{\partial X} - v_2^* \frac{\partial t_1^*}{\partial y} - w_2^* \frac{\partial t_1^*}{\partial z}, \tag{2.61}$$

with upstream condition

$$u_1^* = \epsilon u_{st}, \quad v_2^* = \epsilon v_{st}, \quad w_2^* = \epsilon w_{st}, \quad t_1^* = \epsilon t_{st} \quad \text{for } X = 1, \tag{2.62}$$

wall condition

$$u_1^* = v_2^* = w_2^* = \frac{\partial t_1^*}{\partial y} = 0 \quad \text{for } y = 0, \tag{2.63}$$

and matching condition

$$u_1^* = \frac{\partial v_2^*}{\partial y} = w_2^* = t_1^* = 0 \quad \text{for } y = \infty. \tag{2.64}$$

Equations (2.57)–(2.64) are parabolic in the downstream direction and are readily solved using the above mentioned marching scheme. The nonlinearity of the right-hand-side terms presents no difficulty in principle since the solution scheme is an iterative one, but the iterations necessary to achieve a converged solution increase significantly.

The strongly nonlinear solution of the inner problem can be summarized as

$$U = u_1^0 + u_1^* + O(Gr_L^{*\,-1/5}), \tag{2.65}$$

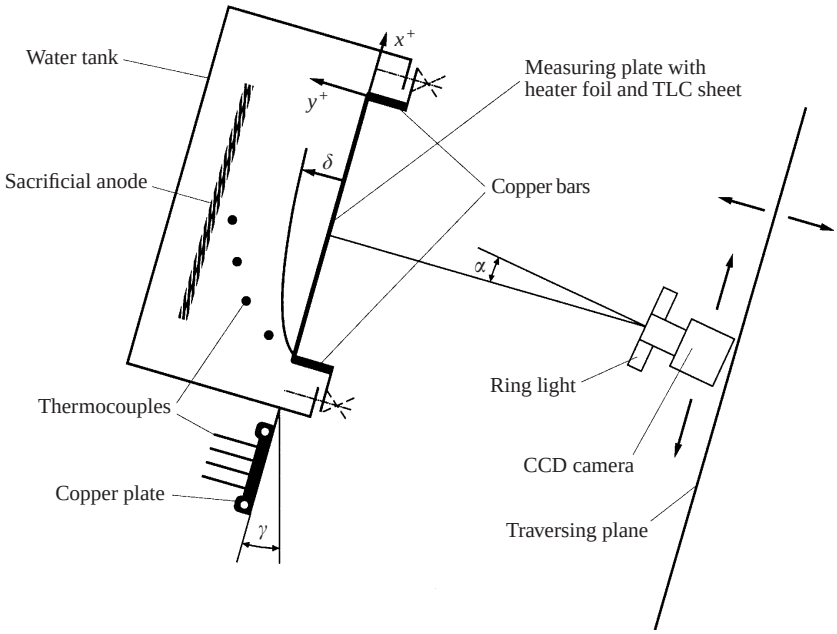

FIGURE 3. Sketch of the experimental apparatus.

$$V = 0 + O(Gr_L^{*\,-1/5}), \tag{2.66}$$

$$W = 0 + O(Gr_L^{*\,-1/5}), \tag{2.67}$$

$$P = const. + O(Gr_L^{*\,-1/5}), \tag{2.68}$$

$$T = t_1^0 + t_1^* + O(Gr_L^{*\,-1/5}), \tag{2.69}$$

with

$$X, y, z, \text{ const.} = O(1).$$

Local Nusselt numbers follow from

$$Nu = Gr_L^{*\,1/5} X\{t_1^0(X,0) + t_1^*(X,0,z) + O(Gr_L^{*\,-1/5})\}^{-1} \tag{2.70}$$

and Nu_{gr}, Gr^*, N^* follow from equations formally identical to (2.49)–(2.51).

3. Experimental method

Only a brief outline of the experimental method is given here. Details can be found in Jeschke (1998) and Jeschke *et al.* (2000). As sketched in figure 3 a 74 cm × 47 cm × 38 cm Plexiglas water tank is used. The tank's bottom plate is removable and holds the 30 cm wide and 50 cm long measuring section which is composed of a thin stainless steel foil, laid above a polyester foil coated with thermochromic liquid crystals (TLCs) and a black backing paint, a thin layer of silicone oil, and the supporting Plexiglas plate. A new vacuum technique (Jeschke, Biertümpfel & Beer 1998*b*) provides a compact composite of the layers, perfectly flat and free of wrinkles over the whole measuring section and during all heating conditions of the steel foil that produces the uniform heat flux boundary condition. The vacuum between the steel foil and the copper bars to which the d.c. voltage is applied also provides a very good and homogeneous electric contact. At the upstream end this gives rise to

a spanwise homogeneous heat flux $\dot{q}_w$ abruptly starting at $x^+ = 0$ and being zero for $x^+ < 0$ where the large area of the copper bar in good thermal contact with the ambient water leads to a constant wall temperature $T_w = T_\infty$. Thereby, the upstream boundary condition as specified in figure 2 and equations (2.8) and (2.9) is satisfied as well as possible with the least possible thermal and fluid flow disturbances, which is important for the primary stability problem.

Surface temperatures T_w are deduced from the TLCs colour distribution which is videographed from behind the tank with the aid of a CCD video camera at a resolution of 768×574 pixels. With the camera lens type used this permits a resolution of up to $\approx 22\,000$ measuring points (pixels) per cm^2 or ≈ 15 pixels per mm in both surface directions. A copper plate mounted on the outside of the tank, within which a defined linear temperature distribution is produced, is used for the TLC colour-to-temperature calibration. Using this calibration the measuring section's TLC colour distribution is transformed into surface temperatures and subsequently into heat transfer coefficients, Nusselt numbers etc., in almost real time by a computer-based data processing system including a colour space conversion. Surface temperatures are estimated to be accurate up to $\pm 0.15\,^\circ\mathrm{C}$ in addition to the accuracy of the thermocouples which is of a similar magnitude. Thermocouples within the tank are used to measure the far-field temperature T_∞ and to check the allowable temperature stratification. The whole apparatus shown in figure 3 can be rotated through 360° allowing easy investigation of arbitrary angles of inclination γ.

In addition to the TLC thermography an electrochemical flow visualization method, previously used by, amongst others, Sparrow & Husar (1969), is employed. The application of this method is described in Jeschke, Biertümpfel & Beer (1998*a*).

4. Results

4.1. *Standard case*

The theoretical results are presented exclusively for one standard case that is used to outline the general physics of the flow. For this standard case the upstream conditions, as needed for the weakly nonlinear marching solution (equation (2.32)) and the strongly nonlinear one (equation (2.62)), are taken from the so-called local analysis of equations (2.27)–(2.34). For this analysis a (modified) parallel flow approximation for the basic flow is made such that the coefficients $u_1^0, \partial u_1^0/\partial X, \ldots$ in equations (2.27)–(2.31) are locally applied at $X = 1$. The equations are then susceptible to a separation of variables solution. Since the kinematics of the primary instability mode are found in § 4.2 to be characterized by steady, downstream growing, and counter-rotating longitudinal vortices of constant dimensional wavelength λ, this separation of variables solution is made in the familiar form

$$u_1^* = u_{st} = \bar{u}(y)\cos(\alpha z)\exp\int \beta\,\mathrm{d}X, \tag{4.1}$$

$$v_2^* = v_{st} = \bar{v}(y)\cos(\alpha z)\exp\int \beta\,\mathrm{d}X, \tag{4.2}$$

$$w_2^* = w_{st} = \bar{w}(y)\sin(\alpha z)\exp\int \beta\,\mathrm{d}X, \tag{4.3}$$

$$p_3^* = p_{st} = \bar{p}(y)\cos(\alpha z)\exp\int \beta\,\mathrm{d}X, \tag{4.4}$$

$$t_1^* = t_{st} = \bar{t}(y)\cos(\alpha z)\exp\int \beta\,\mathrm{d}X. \tag{4.5}$$

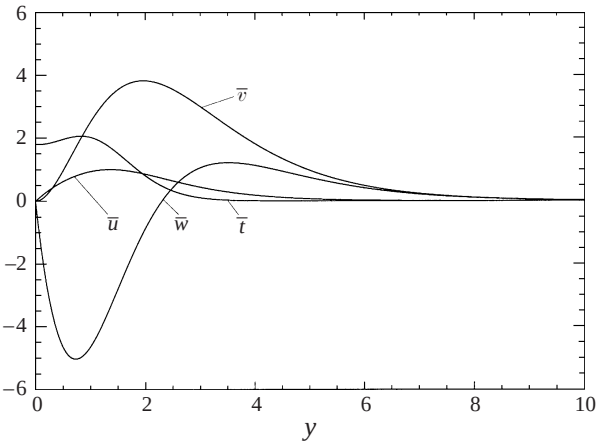

FIGURE 4. Normal-mode eigenfunctions for standard case upstream conditions.

The integral over X is such that it becomes 0 at $X = 1$ irrespective of β. Inserting (4.1)–(4.5) into (2.27)–(2.34) then leads to a linear eigenvalue problem with α, N_L^*, and β being the eigenvalues and $\bar{u}, \bar{v}, \bar{w}, \bar{p}, \bar{t}$ the eigenfunctions. The dimensionless wavenumber α is defined as $\alpha = 2\pi LGr_L^{*-1/5}/\lambda$. This so-called normal-mode solution is provided in Jeschke (1998).

Using the normal-mode solution to specify the upstream conditions needs some justification. Hall (1983) has shown that in Görtler flow, apart from the high-wavenumber limit, the local normal-mode eigenvalue solution cannot be formally justified for finding neutral stability. The same should also apply for the natural convection case treated here. However, Kalburgi, Mangalam & Dagenhart (1988) and Day, Herbert & Saric (1990) compare the local analysis to Hall's initial value approach. They show that with the marching solution, after some downstream distance more or less arbitray initial values converge to flow patterns and growth rates very similar to the normal-mode solution, and vice versa: using the normal-mode solution as initial conditions, the marching solution converges over a shorter streamwise distance to solutions that are consistent with the full equations rather than with arbitrary initial conditions. Since it clearly is not our purpose to find neutral stability but to concentrate on the nonlinear behaviour further downstream, the *ad hoc* nature of the parallel flow approximation is therefore accepted and the normal-mode solution, applied somewhat beyond the neutral curve at $\beta = 0.93$, is taken as initial condition for the marching solution. This practice has also been applied by Lee & Liu (1992) and Benmalek & Saric (1994) for a similar purpose in Görtler flow.

In summary, the upstream conditions for the standard case are taken to be

$$N_L^* = 14.2711, \quad \alpha = 0.7800, \quad \beta = 0.9321, \quad \epsilon = 0.0002, \quad Pr = 5.414, \tag{4.6}$$

with the corresponding eigenvectors given in figure 4. The standard cross-sectional computational domain for the marching solution spans half a vortex wavelength with 30 grid points in the z-direction and 40 in the y-direction which are adequately concentrated near the wall. The downstream distance from $X = 1$ to $X = 10$ is covered with 250 grid points. Symmetry conditions are applied on the z-boundaries. Computation times are in the range of a few minutes on a regular PC for the five-term weakly nonlinear expansion as well as for the nonlinear approach. For clarity, results are presented only for the nonlinear approach. The weakly nonlinear results

duplicate the nonlinear ones until the end of the transition where the weakly nonlinear approach breaks down (see Jeschke 1998).

For the heat transfer measurements presented in figures 8, 10 and 11 the standard system setting defined by

$$\gamma = 25^\circ, \quad \dot{q}_w = 5268.7\,\mathrm{W\,m^{-2}}, \quad T_\infty = 22.9\,^\circ\mathrm{C}, \tag{4.7}$$

is applied. The measuring plate's TLC image is videographed section-wise. Five sections of 6 cm × 8 cm are taken covering the downstream distance from $x^+ = 3$ cm to $x^+ = 33$ cm at a spanwise width of 8 cm. Each of the sections is measured with a resolution of ≈ 10 measuring points per mm in both surface directions giving a total of $\approx 1\,200\,000$ measuring points. The film temperature, averaged over all of them, is found to be $\approx 30\,^\circ$C for which all the fluid properties of water are evaluated and which corresponds to $Pr = 5.414$ as used for the theoretical results. For each curve in figure 8 approximately 250 measuring points in the z^+-direction, covering ≈ 3.5 wavelengths, are depicted. Each of these ≈ 250 measuring points is downstream-averaged over 20 pixels (corresponding to $\Delta x^+ \approx 2$ mm) for noise reduction but no further smoothing or filtering is applied. The downstream averaging is justified by the flow's long-scale downstream variation, characterized by L. However, no spanwise averaging is performed, thereby keeping the high resolution in the spanwise direction which is associated with a short scale variation corresponding to the typical length $\lambda/2 = O(LGr_L^{*-1/5})$. For figure 11 approximately 2200 measuring points in the downstream direction are taken, each of which is averaged over the ≈ 250 pixels in the z^+-direction shown in figure 8 (no downstream averaging). This gives such a smooth curve that it is necessary to artificially magnify the experimental scatter to remain visible.

From equations (4.6) and (4.7)

$$Gr_L^* = \left(\frac{N_L^*}{\tan\gamma}\right)^5 \tag{4.8}$$

can be evaluated and equation (2.50) then brings the theoretical downstream measure X in relation to the experimental downstream measure Gr^*. As a reference, the basic flow Nusselt number Nu_{gr} from equation (2.49) and the turbulent Nusselt number Nu_{turb} taken from the correlation from Vliet (1969)

$$Nu_{turb} = 0.302(Gr^* Pr)^{0.24} \tag{4.9}$$

are plotted in the figures for the heat transfer results.

4.2. *Kinematics*

The velocity vector plots of figure 5(*a*) reveal that the longitudinal vortices are composed of a pair of streamwise-oriented, counter-rotating vortices having a periodicity in the span-wise direction with a wavelength λ encompassing two neighbouring vortices. This wavelength is constant downstream as clearly can be seen in the TLC visualization in figure 14. A videographed sequence of pictures similar to figure 14 and the cross-stream flow visualization of figure 6 prove that the vortices are steady up to the beginning of secondary instabilities. But the vortex instability is of the convective type and the disturbance velocities associated with the vortices grow downstream, starting from an initial upstream value.

The vortices are confined to the boundary layer since only there does a heavy top unstable temperature layer exist. Within this boundary layer the cross-stream disturbance velocities, which are smaller than the mainstream disturbance velocities by the factor $Gr^{*-1/5}$, alternately move near-wall fluid away from the wall in the

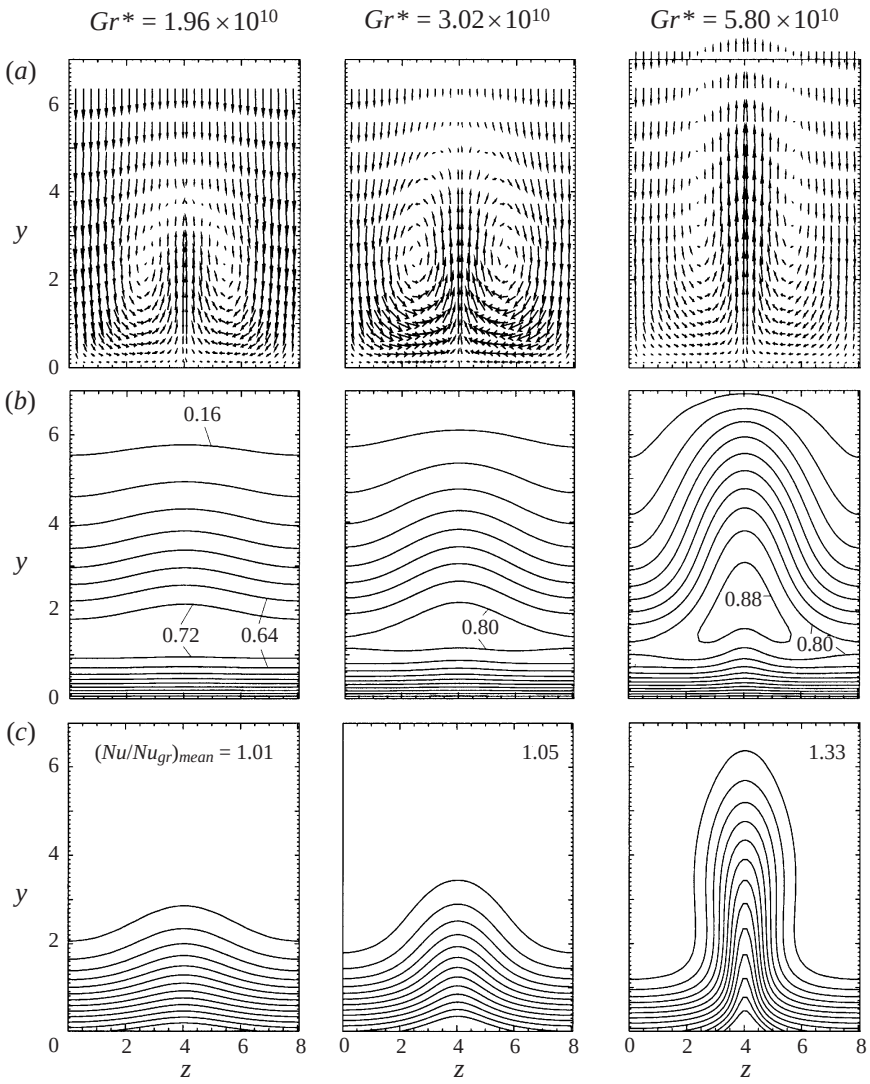

FIGURE 5. (*a*) Downstream development of cross-stream velocities V, W. (*b*) Contour plots of downstream velocity component U. Values range from 0.16 to 0.88 in steps of 0.08. (*c*) Development of isothermals T. Values range from 0.125 to 1.625 in steps of 0.125. $(Nu/Nu_{gr})_{mean}$ is mean ratio of Nusselt number and basic flow Nusselt number as in figure 9. Each set of plots is for the standard case for three different values of the Grashof number.

upwash zone and far-field fluid towards the wall in the downwash zone. The result is a wavy boundary layer structure comprising a sequence of thick and thin portions in the span-wise direction which becomes increasingly pronounced in the downstream direction. The wavyness of the velocity and temperature boundary layers is clearly seen in figure 5(*b*) and 5(*c*), respectively.

A closer look at the velocity vector plots in figure 5(*a*) and the pathlines of figure 7 reveals the motion of the fluid particles. Far upstream the flow is dominated by the two-dimensional basic state which is characterized in the cross-sectional plane by far-field fluid being moved towards the wall over the whole span to account for the fluid swept away within the boundary layer in the downstream direction.

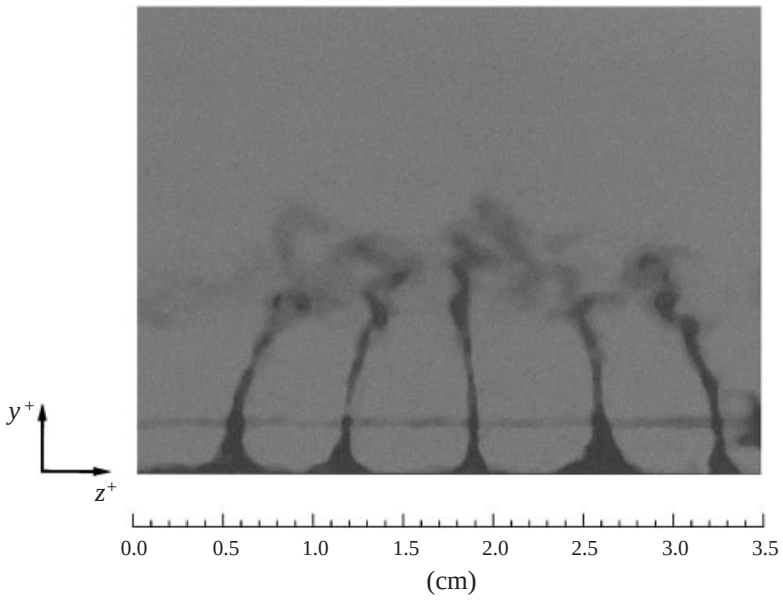

FIGURE 6. Flow visualization (printed in black and white) for $\gamma = 25°$ showing the view along x^+; dark areas represent streaklines of former near-wall particles.

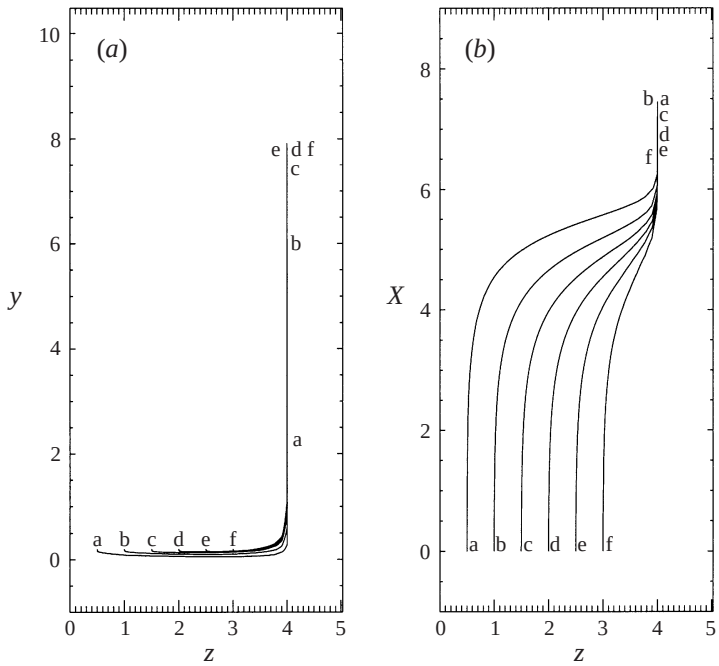

FIGURE 7. Pathlines for the standard case. Letters identify corresponding start and finish of pathlines; z ranges over half a wavelength.

In this regime the fluid particles are merely pushed towards the wall while being convected downstream with no change in spanwise position. Further downstream, with developing vortical disturbances, these particles travel in the spanwise direction parallel to the wall towards the upwash zone where they are convected away from the

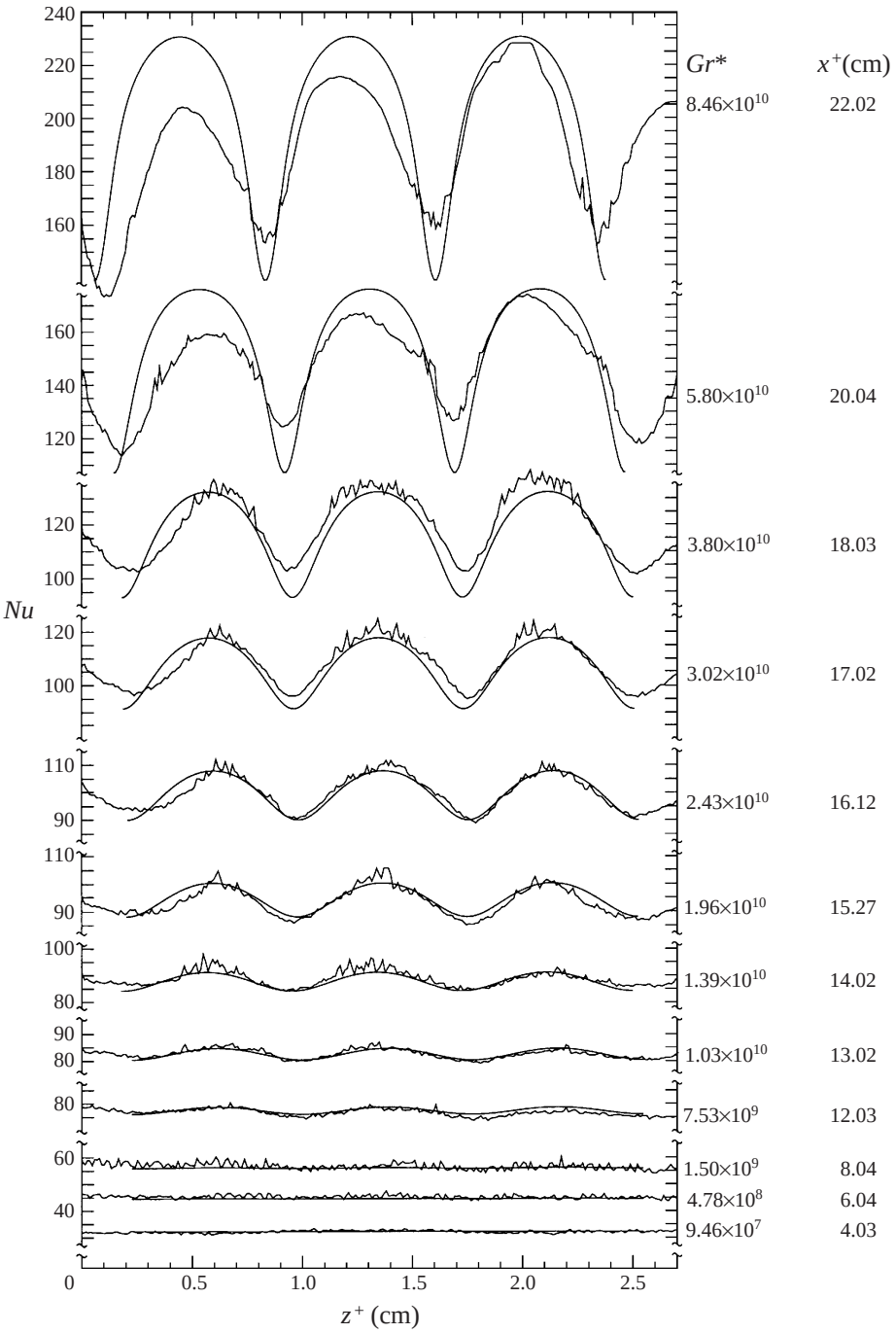

FIGURE 8. Downstream development of Nusselt numbers for the standard case. Noisy curves correspond to experiments, each line drawn from approximately 250 measuring points in the z^+-direction. Smooth curves are the theoretical results. For better comparison, the theoretical curves are shifted in the spanwise direction along with the experimental ones which drift to the left at higher Gr^* as a reaction to a sinuous mode secondary instability.

wall until finally their wall-normal movement is stopped by the opposing incoming far-field fluid. Thus, near-wall fluid particles do indeed only turn through 90° and do not spiral as is generally suggested (e.g. Zuercher *et al.* 1998). This can clearly be seen from the calculated pathlines in figure 7. Because of this motion, only streaky upwash zones are seen in the flow visualization of figure 6 and not the mushroom structure familiar from the Görtler case (Ito 1987). For the visualization in figure 6 the flow is videographed along the mainstream direction and the dark areas represent streaklines of the former upstream near-wall fluid which is coloured there, using the electrochemical technique mentioned in § 3. The streaklines of the flow visualization, therefore, directly correspond to the calculated pathlines in figure 7 in this steady-state situation and the agreement is convincing.

For higher Grashof numbers in figure 5(*a*) the downwash zone can be seen to be wider than the upwash zone. This is a result of the nonlinear effects associated with the vortices disturbance velocities and temperatures. This nonlinear behaviour is seen only after a relatively long linear downstream vortex growth during which upwash and downwash are equally wide and the vortices merely lead to a spanwise, periodic, harmonic variation of the flow without an increase of integral parameters (such as mean heat transfer coefficients, cf. figure 9) over the undisturbed values. It is the widening of the downwash zone and the deviation from the harmonic variation in the nonlinear regime which are responsible for the increase of integral values. In addition to this, only in the nonlinear regime do the inflectional velocity profiles and strong shear layers develop which destabilize the secondary instabilities, finally leading to turbulence. Thus, it is because of the nonlinear effects that the subject of longitudinal vortices receives so much attention.

4.3. *Heat transfer*

The effects on heat transfer are closely related to the extent to which the development of the temperature boundary-layer thickness becomes distorted by the vortical disturbances. These effects are qualitatively seen in the TLC image of figure 14. Far upstream the small boundary-layer thickness of the two-dimensional basic flow leads to such high heat transfer values that the wall temperature falls below the TLCs minimum activation temperature. This causes the TLCs to become transparent and the black backing paint to shine through. Further downstream the continuous thickening of the boundary layer leads to successively lower heat transfer values (higher wall temperatures) and thereby successively shorter dominant wavelengths reflected from the TLCs, changing their colour from red, yellow to green. This mean trend is superposed by a spanwise periodicity, caused by the developing vortices and becoming continuously more pronounced down-stream, of alternately high heat transfer values (red, yellow) in the thinned boundary-layer downwash zones and low heat transfer values (green) in the thickened boundary-layer upwash zones.

This situation is quantitatively depicted in figure 8 revealing a very good agreement between theoretical and measured spanwise Nusselt number distributions. Up to $Gr^* = 1.50 \times 10^9$ practically no spanwise deviation from the basic flow Nusselt numbers is observed. From then on, until about $Gr^* = 1.96 \times 10^{10}$, a region follows where a downstream-growing spanwise variation can be observed with the upwash heat transfer clearly falling below the basic flow value and the downwash heat transfer exceeding it, as can be seen in figures 9 and 10. However, this remains the linear region where the vortical flow is governed (to a large extent) by the first-order linear perturbation equations of § 2.2.2 leading to equally wide up- and downwash zones with a decrease (upwash) and increase (downwash) of heat transfer values of equal

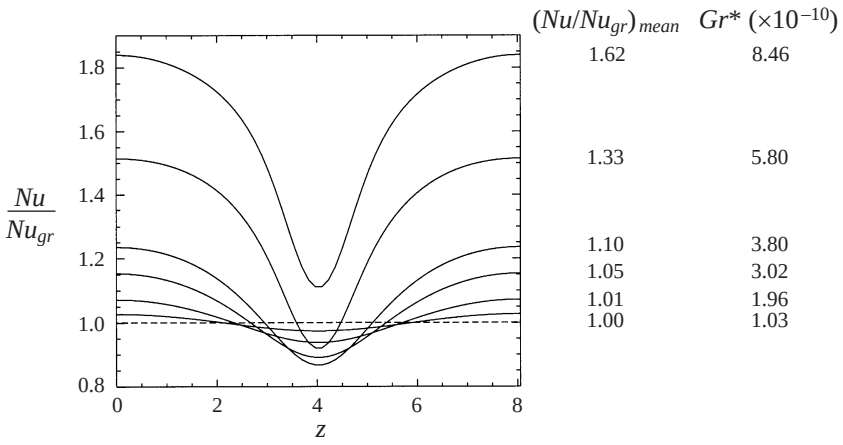

FIGURE 9. Development of ratio of Nusselt number and basic flow Nusselt number for the standard case. $(Nu/Nu_{gr})_{mean}$ is the ratio averaged over one wavelength.

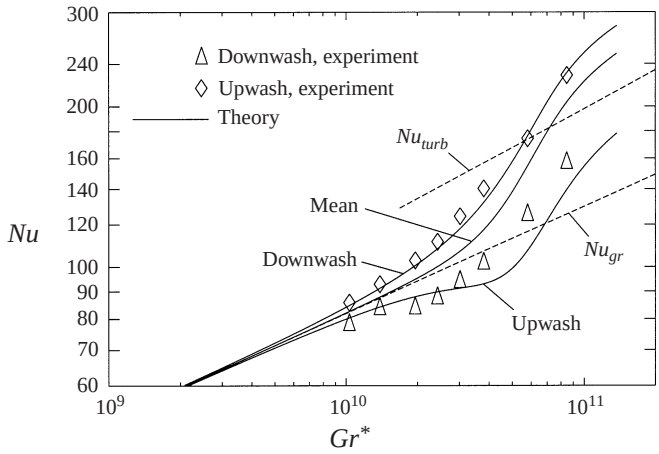

FIGURE 10. Downstream development of mean Nusselt numbers and those for the up- and downwash zones for the standard case: △, experimental minima between $15 < z^+ < 19$ mm of figure 8; ◇, maxima between $19 < z^+ < 24$ mm of figure 8. Nu_{gr} from equation (2.49) and Nu_{turb} from equation (4.9).

amounts in both zones. As a result, the vortices lead to practically no net increase in heat transfer, which is proven by the theoretical results depicted in figure 9 which give an increase of only factor 1.01 at $Gr^* = 1.96 \times 10^{10}$ over the basic flow heat transfer value. This is clearly confirmed by the experimental results shown in figure 11.

After this long linear vortex growth period without effects on mean heat transfer values the nonlinear region, traditionally governed by nonlinear equations such as the strongly non-linear approach of § 2.3, follows from about $Gr^* = 1.96 \times 10^{10}$ onwards. It is characterized by a widening of the downwash zone relative to the upwash zone (cf. figures 8, 9) and an increase of heat transfer values in the downwash zone compared to the basic flow values that is stronger than the decrease in the upwash zone (cf. figures 9, 10). Both effects lead to an increase of mean heat transfer values, which, with very good agreement between theory and experiment, gradually change from laminar to turbulent values as can be seen in figure 11. The vortices thus lead to a heat transfer

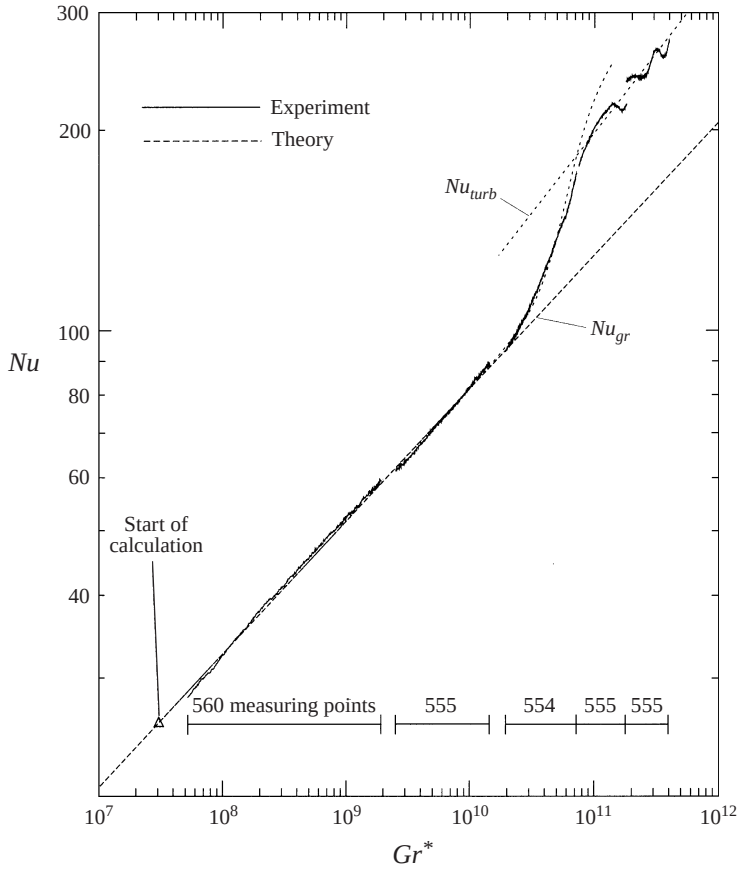

FIGURE 11. Downstream development of mean Nusselt numbers for the standard case. Nu_{gr} from equation (2.49) and Nu_{turb} from equation (4.9).

increase by the factor 1.33 at $Gr^* = 5.80 \times 10^{10}$ over the basic flow value (figure 9). This nonlinear behaviour can also be seen qualitatively in figure 14 where, far enough downstream, the upwash zones degenerate to small strips and the dominating black colour, caused by the wall temperatures falling below the TLC minimum activation temperature as a result of the high downwash heat transfer, clearly shows the mean increase of heat transfer. Finally, from about $Gr^* = 5.80 \times 10^{10}$ on, with the start of the unsteady secondary instabilities, the hitherto good agreement in figure 8 and figure 11 between experiment and theory vanishes since the theory does not capture unsteadiness. However, at that point the heat transfer values have already reached turbulent levels. This makes clear that the vortices account for practically all of the increase from laminar to turbulent values during the transition process whereas the secondary instabilities only exert a minor effect on heat transfer.

These effects of the vortices on heat transfer are analogous to what is observed in the Görtler case and the mixed convection case (Jeschke 1998). However, in these cases the heat transfer values differ significantly more in the up- and downwash zones and mean values increase by up to factors 3–4 over the basic flow values at the end of the transition for similar Prandtl numbers (compare figures 9 and 10 with the analogous figures presented by Jeschke (1998) for the other cases). This can be attributed to the fact that the vortices generally account for the transition from

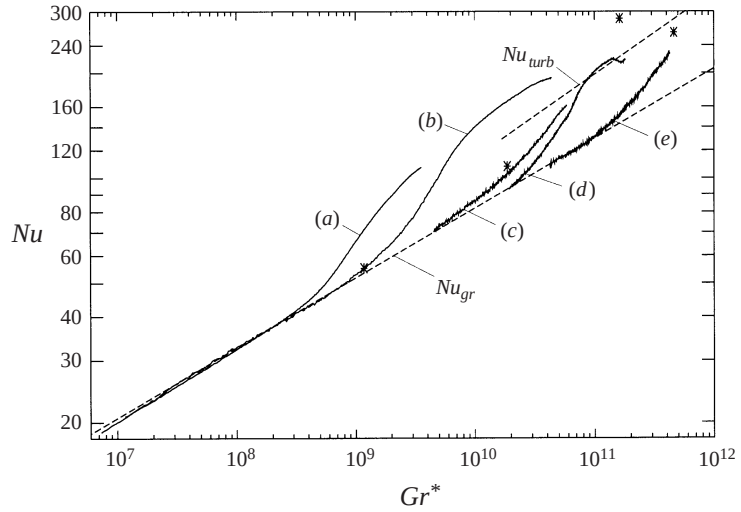

FIGURE 12. Downstream development of mean Nusselt numbers for different inclination angles γ. Material properties evaluated at 30 °C corresponding to $Pr = 5.414$. (*a*) $\gamma = 50°$, $\dot{q}_w = 6157.8\,\mathrm{W\,m^{-2}}$, $T_\infty = 22.1$°C, (*b*) $\gamma = 40°$, $\dot{q}_w = 6522.1\,\mathrm{W\,m^{-2}}$, $T_\infty = 23.4$ °C, (*c*) $\gamma = 30°$, $\dot{q}_w = 4176.0\,\mathrm{W\,m^{-2}}$, $T_\infty = 25.3$ °C, (*d*) $\gamma = 25°$, $\dot{q}_w = 5268.7\,\mathrm{W\,m^{-2}}$, $T_\infty = 22.9$ °C, (*e*) $\gamma = 20°$, $\dot{q}_w = 6157.8\,\mathrm{W\,m^{-2}}$, $T_\infty = 23.5$ °C; *, $\gamma = 29°$, $\dot{q}_w = 2291\,\mathrm{W\,m^{-2}}$, Shaukatullah & Gebhart (1978). Nu_{gr} from equation (2.49) and Nu_{turb} from equation (4.9).

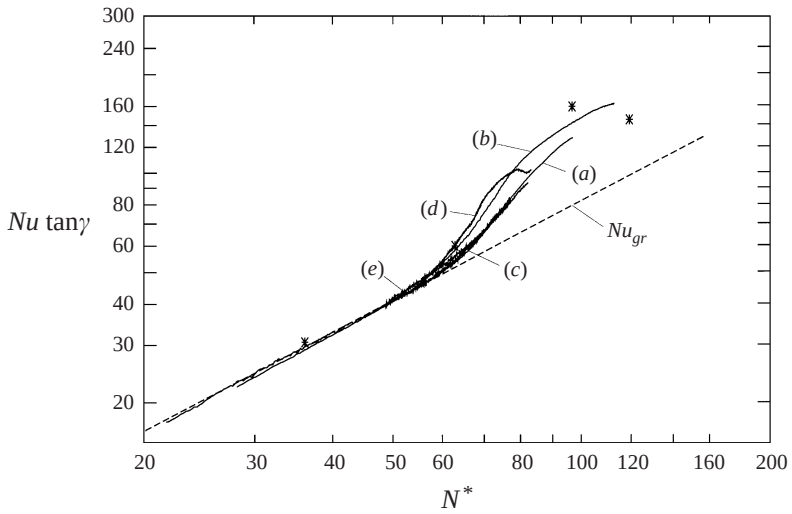

FIGURE 13. Development of mean Nusselt numbers for different inclination angles γ as in figure 12 but as a function of the stability parameter $N^* = \tan\gamma Gr^{*1/5}$. Nu_{gr} from equation (2.49).

laminar to turbulent values which are larger in these cases by the factors mentioned above.

Finally, as depicted in figures 12 and 13, the effect of the inclination angle γ is investigated. The five angles $\gamma = 20°$, $25°$, $30°$, $40°$, $50°$ are used and Nusselt numbers are determined for each of them from at least 500 downstream measuring points, each of which is spanwise averaged over $\approx$ 300–400 pixels. As is seen in figure 12, the transition Grashof number decreases with an increasing destabilizing

wall-normal buoyancy force at increasing inclination angles. This causes transition to begin as early as at $Gr^* \approx 3 \times 10^8$ for $\gamma = 50^\circ$ whereas for $\gamma = 20^\circ$ it begins at $Gr^* \approx 1 \times 10^{11}$. However, the start of transition is correlated well by the stability parameter $N^* = \tan\gamma Gr^{*1/5}$, as can be seen in figure 13. It is also noticeable that for large inclination angles the Nusselt numbers exceed the turbulent values at the end of the transition and later approach the turbulent values 'from above', cf. figure 12. With the help of the flow visualization this is observed to be the result of a sudden boundary-layer separation in the upwash zones at the end of the transition which pushes cold far-field fluid towards the wall; this does not occur for smaller inclination angles.

4.4. *Secondary instabilities*

Figures 14, 15 show TLC visualizations of the linear and nonlinear regimes. In the strongly nonlinear regime, the vortex distortion leads to inflectional profiles of the downstream velocity component and high-shear layers around the upwash section. These provoke wave-like secondary instabilities of the Tollmien–Schlichting and the Kelvin–Helmholz type which have been thoroughly investigated for the Görtler case (Floryan 1991; Saric 1994).

A strongly distorted streamwise velocity contour well within the nonlinear regime at $Gr^* = 5.80 \times 10^{10}$ is shown in figure 5(*b*). High values of $\partial u/\partial z$ at the upwash sides then lead to the two wave modes shown in the TLC visualizations of figure 15. The first is the sinuous mode characterized by two neighbouring waves being in phase, which is approximately the case in figure 15(*a*), and the second is the varicose mode with a phase shift of half a period which is depicted in figure 15(*b*). In qualitative agreement with stability analyses of the Görtler case, the sinuous mode is observed more frequently than the varicose one in the experiments of this study. In fact, a sinuous mode can be identified in the Nusselt number distribution of figure 8, where the experimental curves drift to the left from approximately $Gr^* = 5.80 \times 10^{10}$ onwards. This leads to the wavy mean Nusselt number distribution in figure 11 which is caused by vortices drifting in and out of the measuring section. (The discontinuity in the distribution of figure 11 comes from the fact that the measurements within the succeeding sections are performed at a time difference of several seconds during which several waves pass through.)

Horseshoe vortices are not observed in the flow visualizations and TLC images of this study. As in the Görtler case, one would expect them to be generated from spanwise vortices arising from strong gradients $\partial u/\partial y$ on top of the upwash (cf. figure 5*b*) through a Kelvin–Helmholz instability (Floryan 1991). The lack of horseshoe vortices could be related to the fact that the sense of rotation of the spanwise vortex would be different in the natural convection case, since, in contrast to the Görtler case, the upwash carries the high-momentum fluid.

A frequently observed third instability is depicted in figure 15(*c*). The TLC visualization suggests that two neighbouring vortices merge thereby effectively doubling the wavelength. However, the flow visualizations reveal that for larger inclination angles ($\gamma \geqslant 40^\circ$) similar TLC images are produced as a result of spanwise shifting of vortices owing to local boundary-layer separations. In effect, the hot upwash legs are seen to merge into plumes that lift off the plate allowing the neighbouring vortices to move in the spanwise direction. The schlieren pictures in Zuercher *et al.* (1998) for $\gamma = 40^\circ$ and $\gamma = 60^\circ$ show a merger of the hot-upwash schlieren streaks which is likely to be caused by the same effect rather than by true merging of vortices. For these larger inclination angles the vortex inception and subsequent breakdown occurs

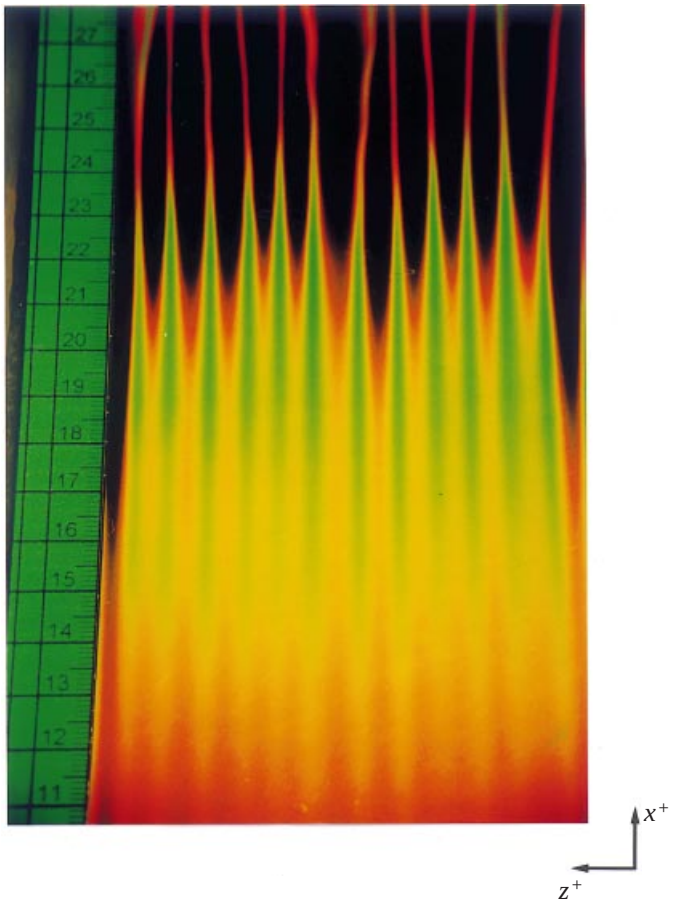

FIGURE 14. Liquid-crystal wall temperature visualization of vortex development for $\gamma = 20°$; the view is normal to the plate from behind the tank.

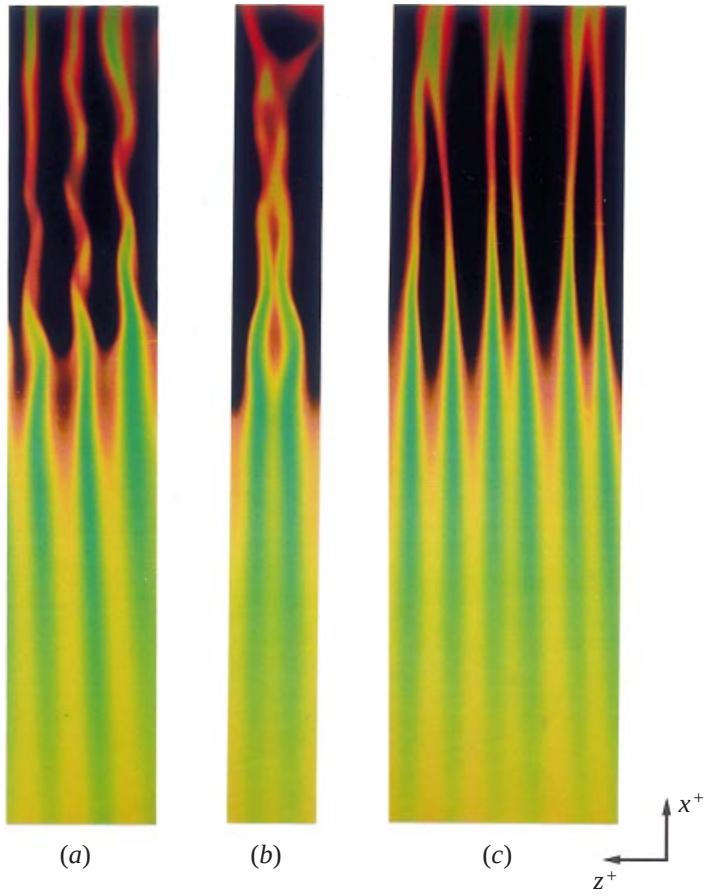

FIGURE 15. Liquid-crystal wall temperature visualization of secondary instabilities for $\gamma = 20°$; (*a*) sinuous instability, (*b*) varicose instability, (*c*) merging of two upwash zones.

for such low Grashof numbers (cf. figure 12) that there is only a weak destabilization of the wave modes. This should explain why the wave modes are not dominant in the schlieren pictures of Zuercher *et al.* (1998). However, for $\gamma = 20^\circ$ in figure 15 no boundary-layer separation is observed in our flow visualization, thus supporting the interpretation that for smaller angles vortices frequently indeed 'merge'. However, the wave modes were always dominant in our experiments at lower inclination angles.

5. Conclusions

The linear and nonlinear vortex growth and the breakdown structure through secondary instabilities of a longitudinal vortex system in a natural convection prototype problem is investigated. The thoretical method is based on a formal perturbation method which leads to a consistent set of governing equations for the linear and nonlinear vortex regime. By carrying out an expansion in ϵ within the scope of a new weakly nonlinear approach, a set of linear governing equations is derived so that the nonlinear vortex growth can be calculated from exclusively linear equations. For the natural convection flow of this study the weakly nonlinear approach and an additional strongly nonlinear approach are used to predict for the first time the increase of integral parameters such as mean heat transfer values during the nonlinear transition. TLC thermography is used to provide high-resolution, full-field, highly accurate wall temperature measurements and visualizations for this flow configuration that previously were not available.

The kinematics of the vortices turns out to be analogous to what is known of the Görtler case, but near-wall fluid particles only travel through a 90° bend and do not perform a spiralling motion as is generally suggested. Nonlinear effects are seen only after a relatively long period of linear vortex growth during which the vortices cause a spanwise periodicity of the flow without an increase of integral parameters. The nonlinear interaction of the disturbance quantities then leads to a widening of the downwash zone relative to the upwash zone and a greater increase of heat transfer values in the downwash zone compared to the basic flow values than the decrease in the upwash zone. The result is a gradual increase of mean heat transfer values from laminar to turbulent levels. A comparison between theory and experiment makes clear that the vortices account for practically all of the increase during the transition process whereas secondary instabilities only have a minor effect on heat transfer. These secondary instabilities are destabilized by high-shear layers around the upwash section in the strongly nonlinear regime. Of the two unsteady modes, the sinuous and the varicose, the former is observed more often. In addition, the TLC visualizations frequently suggest a steady merging of two neighbouring vortices.

REFERENCES

Benmalek, A. & Saric, W. S. 1994 Effects of curvature variations on the nonlinear evolution of Görtler vortices. *Phys. Fluids* **6**, 3353–3367.

Black, W. Z. & Norris, J. K. 1975 The thermal structure of free convection turbulence from inclined isothermal surfaces and its influence on heat transfer. *Intl J. Heat Mass Transfer* **18**, 43–50.

Chen, C. C., Labhabi, A., Chang, H.-C. & Kelly, R. E. 1991 Spanwise pairing of finite-amplitude longitudinal vortex rolls in inclined free-convection boundary layers. *J. Fluid Mech.* **231**, 73–111.

Chen, T. S. & Tzuoo, K. L. 1982 Vortex instability of free convection flow over horizontal and inclined surfaces. *Trans. ASME: J. Heat Transfer* **104**, 637–643.

Cheng, K. C. & Kim, Y. W. 1988 Flow visualization studies on vortex instability of natural

convection flow over horizontal and slightly inclined constant-temperature plates. *Trans. ASME: J. Heat Transfer* **110**, 608–615.

Day, H. P., Herbert, T. & Saric, W. S. 1990 Comparing local and marching analysis of Görtler instability. *AIAA J.* **28**, 1010–1015.

Dean, W. R. 1928 Fluid motion in a curved channel. *Proc. R. Soc. Lond.* A **15**, 623–631.

Floryan, J. M. 1991 On the Görtler instability of boundary layers. *Prog. Aerospace Sci.* **28**, 235–271.

Fujii, T. & Imura, H. 1972 Natural-convection heat transfer from a plate with arbitrary inclinations. *Intl J. Heat Mass Transfer* **15**, 755–767.

Goldstein, R. J., Sparrow, E. M. & Jones, D. C. 1973 Natural convection mass transfer adjacent to horizontal plates. *Intl J. Heat Mass Transfer* **16**, 1025–1035.

Görtler, H. 1940 Über eine Dreidimensionale Instabilität Laminarer Grenzschichten an Konkaven Wänden. *Nachr. Ges. Wiss. Göttingen, Math.-Phys. Klasse, Neue Folge I* **2**, 1–26.

Görtler, H. 1958 Über eine Analogie zwischen den Instabilitäten laminarer Grenzschichtströmungen an konkaven Wänden und an erwärmten Wänden. *Ingr. Arc.* **23**, 71–78.

Haaland, S. E. & Sparrow, E. M. 1973 Vortex instability of natural convection flow on inclined surfaces. *Intl J. Heat Mass Transfer* **16**, 2355–2367.

Hall, P. 1983 The linear development of Görtler vortices in growing boundary layers. *J. Fluid Mech.* **130**, 41–58.

Hall, P. 1988 The nonlinear development of Görtler vortices in growing boundary layers. *J. Fluid Mech.* **193**, 243–266.

Hall, P. 1993 Streamwise vortices in heated boundary layers. *J. Fluid Mech.* **252**, 301–324.

Hall, P. & Morris, H. 1992 On the instability of boundary layers on heated flat plates. *J. Fluid Mech.* **245**, 367–400.

Hwang, G. J. & Cheng, K. C. 1973 Thermal instability of laminar natural convection flow on inclined isothermal plates. *Can. J. Chem. Engng* **51**, 659–666.

Ito, A. 1986 Visualization of boundary layer transition along a concave wall. *Proc. 4th Intl Symp. Flow Visualization, Paris* (ed. C. Véret), vol. 33, pp. 339–344. Hemisphere.

Iyer, P. A. & Kelly, R. E. 1974 The stability of the laminar free convection flow induced by a heated inclined plate. *Intl J. Heat Mass Transfer* **17**, 517–525.

Jeschke, P. 1998 Längswirbel in laminaren Grenzschichtströmungen und deren Einfluß auf den Wärmeübergang. PhD thesis, Technische Universität Darmstadt, Fortschr.-Ber. VDI Reihe 7 Nr. 350. Düsseldorf: VDI Verlag.

Jeschke, P., Biertümpfel, R. & Beer, H. 1998*a* Visualization of longitudinal vortices and surface temperatures in a natural convection experiment. *Proc. 8th Intl Symp. Flow Visualization, Sorrento, Italy* (ed. I. Grant). G. M. Carlomagno.

Jeschke, P., Biertümpfel, R. & Beer, H. 1998*b* German Patent No. 198 06 632.6-52.

Jeschke, P., Biertümpfel, R. & Beer, H. 2000 Liquid-crystal thermography for heat-transfer measurements in the presence of longitudinal vortices in a natural convection flow. *Meas. Sci. Technol.* **11**, 447–453.

Kahawita, R. A. & Meroney, R. N. 1974 The vortex mode of instability in natural convection flow along inclined plates. *Intl J. Heat Mass Transfer* **17**, 541–548.

Kalburgi, V., Mangalam, S. M. & Dagenhart, J. R. 1988 A comparative study of theoretical methods on Görtler instability. *AIAA Paper* 88-0407.

King, J. A. & Reible, D. D. 1991 Laminar natural convection heat transfer from inclined surfaces. *Intl J. Heat Mass Transfer* **34**, 1901–1904.

Kitamura, K. & Kimura, F. 1995 Heat transfer and fluid flow of natural convection adjacent to upward-facing horizontal plates. *Intl J. Heat Mass Transfer* **38**, 3149–3159.

Lee, H. R., Chen, T. S. & Armaly, B. F. 1992 Non-parallel thermal instability of natural convection flow on non-isothermal inclined flat plates. *Intl J. Heat Mass Transfer* **35**, 207–220.

Lee, K. & Liu, J. T. C. 1992 On the growth of mushroomlike structures in nonlinear spatially developing Görtler vortex flow. *Phys. Fluids* A **4**, 95–103.

Liu, J. T. C. & Lee, K. 1995 Heat transfer in a strongly nonlinear spatially developing longitudinal vorticity system. *Phys. Fluids* **7**, 559–599.

Lloyd, J. R. 1974 Vortex wavelength in the transition flow adjacent to upward facing inclined isothermal surfaces. In *Heat Transfer*, vol. 3, Paper No. NC1.8, pp. 24–37.

Lloyd, J. R. & Moran, W. R. 1974 Natural convection adjacent to horizontal surface of various platforms. *Trans. ASME: J. Heat Transfer* 443–447.

Lloyd, J. R. & Sparrow, E. M. 1970 On the instability of natural convection flow on inclined plates. *J. Fluid Mech.* **42**, 465–470.

Patankar, S. V. 1980 *Numerical Heat Transfer*. Hemisphere.

Pera, L. & Gebhart, B. 1973 Natural convection boundary layer flow over horizontal and slightly inclined surfaces. *Intl J. Heat Mass Transfer* **16**, 1131–1146.

Saric, W. S. 1994 Görtler vortices. *Ann. Rev. Fluid Mech.* **26**, 379–409.

Shaukatullah, H. & Gebhart, B. 1978 An experimental investigation of natural convection flow on an inclined surface. *Intl J. Heat Mass Transfer* **21**, 1481–1490.

Sparrow, E. M. & Husar, R. B. 1969 Longitudinal vortices in natural convection flow on inclined plates. *J. Fluid Mech.* **37**, 251–255.

Taylor, G. I. 1923 Stability of a viscous liquid contained between two rotating cylinders. *Phil. Trans. R. Soc. Lond.* A **223**, 289–343.

Tien, H. C., Chen, T. S. & Armaly, B. F. 1986 Vortex instability of natural convection flow over horizontal and inclined plates with uniform surface heat flux. *Numer. Heat Transfer* **9**, 697–713.

Van Dyke, M. 1975 *Perturbation Methods in Fluid Mechanics*. Parabolic Press, Stanford.

Vliet, G. C. 1969 Natural convection local heat transfer on constant heat flux inclined surfaces. *Trans. ASME: J. Heat Transfer* **91**, 511–517.

Vliet, G. C. & Ross, D. C. 1975 Turbulent natural convection on upward and downward facing inclined constant heat flux surfaces. *Trans. ASME: J. Heat Transfer*, 549–555.

Yousef, W. W., Tarasuk, J. D. & McKeen, W. J. 1982 Free convection heat transfer from upward-facing isothermal horizontal surfaces. *Trans. ASME: J. Heat Transfer* **104**, 493–500.

Zuercher, E. J., Jacobs, J. W. & Chen, C. F. 1998 Experimental study of the stability of boundary-layer flow along a heated, inclined plate. *J. Fluid Mech.* **367**, 1–25.